

Bowknot-like Zr/La bimetallic organic frameworks for enhanced arsenate and phosphate removal: Combined experimental and DFT studies

Lingchao Kong^a, Jun Zhang^b, Yi Wang^c, Qinlin Yan^a, Jiayu Xu^a, Xi Quan^b, Charles B. Andrews^{a,d}, Zuotai Zhang^a, Chunmiao Zheng^{a,*}

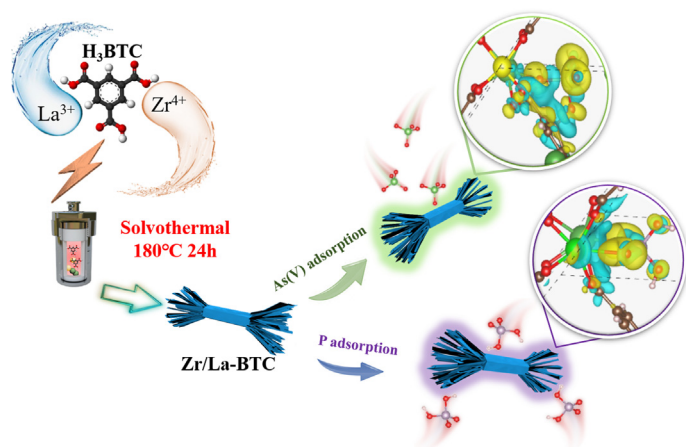
^a State Environmental Protection Key Laboratory of Integrated Surface Water–Groundwater Pollution Control, School of Environmental Science & Engineering, Southern University of Science and Technology, Shenzhen, Guangdong 518055, China

^b State Key Laboratory of Urban Water Resource and Environment, School of Environment, Harbin Institute of Technology, Harbin 150090, China

^c Department of Ocean Science and Engineering, Southern University of Science and Technology, Shenzhen 518055, China

^d S.S. Papadopoulos & Associates, Inc., Rockville, MD 20852, United States

GRAPHICAL ABSTRACT



ARTICLE INFO

Article history:

Received 15 November 2021

Revised 3 January 2022

Accepted 5 January 2022

Available online 10 January 2022

Keywords:

Hazardous oxyanions

Water treatment, Metallic organic framework

Adsorption

Electronic charge density

ABSTRACT

Hazardous oxyanions in water bodies are potentially toxic to aquatic life, and the coexistence of multiple anions aggravates the toxicity. Herein, bowknot-like Zr/La bimetallic organic frameworks (Zr/La-BTC) were developed with superior hazardous oxyanion adsorption capacities, i.e., approximately 102 mg/g for arsenate and 159 mg/g for phosphate, respectively. The molar ratio of Zr to La in Zr/La-BTC plays a significant role in the structure and the adsorption efficiencies. Notably, the experiment-derived adsorption capacities of various Zr/La-BTC samples were consistent with their adsorption energies calculated by density-function theory (DFT). Further mechanism analysis revealed that coordination of Zr/La atoms with the target anion groups occurred during adsorption. The positive shift of binding energies in La 3d and Zr 3d XPS spectra and Bader charge analysis unveiled that back-donation interactions dominated the adsorption process. The reliable adsorption selectivity and reusability of 0.1Zr/La-BTC were verified with anion competition experiments and four adsorption-desorption cycles. Overall, this study provides

* Corresponding author.

E-mail address: zhengcm@sustech.edu.cn (C. Zheng).

significant insight into the design of high-performance bimetallic organic frameworks for the enhanced removal of hazardous oxyanions from water.

© 2022 Elsevier Inc. All rights reserved.

1. Introduction

Excessive hazardous oxyanions in rivers and groundwater have drawn global attention due to their severe toxicity on the ecosystem and public health safety. Human health effects of arsenate, a common oxyanion, include cardiovascular problems, liver malfunctioning, heart diseases, and even cancer [5,35]. Studies have found that the coexistence of phosphate (PO_4^{3-}) with arsenate deteriorates water quality and leads to dramatic fluctuations in the ecological system's balance [44]. Due to the high toxicity of these two oxyanions to aquatic ecosystems, the World Health Organization (WHO) and the United States Environmental Protection Agency (USEPA) recommend that the permissible discharge limitation values for total arsenic and phosphorus in water bodies are 0.01 mg/L [11] and 0.5 mg/L [4], respectively. However, the concentrations of these anionic pollutants in water bodies in Latin America, Pakistan, China, Chile, and India are higher than the average international standards [7,41]. Therefore, there is an urgent need to remove phosphate and arsenate from water to improve water quality and safety.

Adsorption is a suitable technique for removing hazardous aquatic oxyanions due to its cost-effectiveness, convenient operation, and potential selectivity [28]. Although much progress has been achieved in developing various adsorbents for oxyanion removal, such as mesoporous-based materials, red mud, and bioresource materials [1,2,13], the challenges of relatively low adsorption capacity and selectivity still hinder their wide application. Lanthanum (La), a metallic rare-earth element with a specific and robust adsorption affinity for oxyanions, has been widely developed as an agent for enhanced inorganic contaminant elimination [16,48]. It is generally acknowledged that La has an extremely high affinity for arsenate [14]. Thus, considerable La-based adsorbents have been synthesized, such as commercialized La-modified bentonite clay and La hydroxides, etc. [10,39]. Recently, metal-organic frameworks (MOFs) have drawn much attention for their outstanding physical and chemical properties, which creates favorable conditions for adsorbing anionic contaminants [36,37]. Thus, much effort has been devoted to exploring hierarchical nanocomposites with extended properties from the combination of La and MOFs based on their synergic effect [29].

Generally, compared with monometallic La-based MOFs, nanostructured bi-/tri-metallic MOFs display outstanding adsorption efficiency for hydrous oxyanions. Extensive research has shown that MOFs can chelate multiple metal ions and form stable materials by integrating metal nodes, organic linkers, and functional groups [3,26]. Recent evidence suggests that pronounced arsenate removal is achieved by Zr-decorated composites [42]. Therefore, exploring novel Zr/La hybrid MOFs may provide perspectives for future experimental design. Notably, previous experiments revealed that the role of lattice oxygen in oxygen redox reactions could be significantly intensified by doping mixed metals due to the increase in the covalence of the metal–O bond [40]. As the electronegativities of La and Zr are different, the incorporation of La and Zr metals is supposed to induce a change in the covalence of the metal–O bonds, contributing to the enhancement of oxyanion adsorption by accommodating active electrons in oxyanion molecules [40]. However, the endeavor of introducing La and Zr for the generation of novel nanostructured bimetallic organic frameworks has not been reported. In addition, the performance

of phosphate and arsenate adsorption and the underlying mechanism of increased adsorption efficacy of Zr/La hybrid MOFs have not been described clearly.

This study achieved the novel syntheses of Zr/La hybrid MOFs with the organic ligand of benzene tricarboxylic acid by a facile hydrothermal approach. The prepared Zr/La-BTC composites were successfully applied to the removal of phosphate (P) and arsenate [As(V)]. The effect of various Zr/La ratios on the structures and adsorption efficiency was investigated in detail. The enhanced adsorption mechanism was elucidated via FTIR, XPS, and DFT calculations. These insights shed new light on the adsorption interactions between oxyanion contaminants and La- or Zr-based MOFs regarding adsorption energy and charge transfer.

2. Materials and methods

2.1. Materials

Lanthanum nitrate ($\text{La}(\text{NO}_3)_3 \cdot 6\text{H}_2\text{O}$), zirconium nitrate ($\text{Zr}(\text{NO}_3)_4 \cdot 5\text{H}_2\text{O}$), benzene tricarboxylic acid (H_3BTC), potassium dihydrogen phosphate (KH_2PO_4), and N–N–dimethylformamide (DMF) were purchased from Aladdin Chemistry Co. Ltd. Sodium arsenate (Na_3AsO_4) was obtained from Sigma-Aldrich Co. Ltd. Additionally, standard stock solutions of phosphate and arsenate were prepared from KH_2PO_4 and Na_3AsO_4 , respectively. All chemical reagents used in this study were analytically pure.

2.2. Synthesis of the Zr/La-BTC MOFs

A facile hydrothermal approach was adopted to synthesize Zr/La-BTC MOFs [45]. A mixture composed of $\text{La}(\text{NO}_3)_3 \cdot 6\text{H}_2\text{O}$ (x mmol), $\text{Zr}(\text{NO}_3)_4 \cdot 5\text{H}_2\text{O}$ (y mmol, $x + y = 6$), and H_3BTC (3 mmol) was dispersed in 60 mL DMF solution under vigorous stirring for 1 h. Then, the mixture was poured into Teflon-lined reaction kettles for 24-hour heating at 180 °C. After centrifugation and filtration, the collected precipitates were rinsed with DMF and ethanol three times and air-dried at 60 °C overnight. The resultants were denoted as 0.1Zr/La-BTC ($x = 5.4$, $y = 0.6$), 0.3Zr/La-BTC ($x = 4.8$, $y = 1.2$) and 0.5Zr/La-BTC ($x = 3$, $y = 3$) according to the amount of La substituted by Zr species. La-BTC and Zr-BTC were synthesized using the same procedure without introducing mixed metals.

2.3. Batch adsorption experiments

The adsorption isotherm experiments were conducted using 50 mL P and As(V) solutions with a concentration gradient from 1 to 200 mg/L. After adding adsorbent at a dose of 0.05 g, the mixture was placed in a thermostatic air bath shaker for 24 h at 210 rpm. Subsequently, the supernatant was obtained by filtering the suspensions with a 0.45 μm membrane for subsequent anion concentration detection. The P and As(V) concentrations in solutions were detected via UV/vis spectroscopy with the molybdenum blue method and coupled plasma-optical emission spectrometry (ICP-OES, iCAP RQ, ThermoFisher), respectively. According to the concentration changes over the adsorption period the P and As(V) adsorption capacities of diverse adsorbents were calculated as described in [Supplementary Material](#). Each experimental data point in this study was represented as the average of three

repeated experiments. Langmuir and Freundlich models were employed to fit the adsorption isotherm data and the equations are shown in Table S1. At the beginning of the kinetic adsorption experiment, 0.01 g adsorbent was dispersed into a 50 mL solution with an assigned P or As(V) concentration. Afterward, 2 mL of liquid was extracted at each prearranged time point (2, 5, 10, 30 min, and 1, 2, 6, 12, 24 h) for concentration measurement. The experimental kinetic data were fitted with pseudo-first-order and pseudo-second-order models and the corresponding equations are shown in Table S2.

Competitive adsorption experiments were performed to evaluate the selectivity of Zr/La-BTC for phosphate and arsenate adsorption. Coexisting anions (NO_3^- , SO_4^{2-} , Cl^- , HCO_3^{2-} and F^-) were spiked into 50 mg/L P and As(V)-containing solutions at various strengths (5, 10, and 50 mg/L). The effect of pH values on adsorption efficiencies was also investigated by adjusting the initial solution pH values ranging from 3 to 10 with 0.01 mol/L NaOH and HNO_3 reagents. Furthermore, the practicality of Zr/La-BTC for water treatment was tested on a groundwater sample collected from a monitoring well (113° 57'33.64"E, 22°32'19.53"N) in Shenzhen, China. The main water quality characteristics of the water sample are shown in Table S3. The adsorption tests for phosphate and arsenate removal were conducted using the same procedure mentioned above (adsorbent dose: 0.02 g, solution volume: 50 mL). The equilibrium concentrations of P and As(V) in these mixture were detected after adsorption duration of 24 h.

Adsorption-desorption cycle experiments were conducted to examine the reusability of the as-prepared Zr/La-BTC. A preliminary adsorption experiment was performed by adding 0.2 g adsorbent into 50 mL solutions with 20 mg P/L and 5 mg As/L, respectively. Afterward, the exhausted adsorbent was collected and treated with 0.1 mol/L NaCl/NaOH overnight under vigorous agitation to desorb the loaded phosphate and arsenate. The regenerated sample was then treated by filtration, rinsed with deionized water until a neutral pH, air-cured, and subsequently reused for the subsequent adsorption analysis. Four successive adsorption-desorption cycles were carried out, and the corresponding adsorption performances were also investigated.

2.4. Characterization and analytical methods

The surface morphological analysis of the as-prepared Zr/La-BTC MOFs was conducted by scanning electron microscopy (SEM, Nova NanoSEM450 FEI, USA), an attached dispersive X-ray system (EDX), and transmission electron microscopy (TEM, Tecnai F30, Philips-FEI, Netherlands). X-ray diffraction (XRD) patterns were collected via an X-ray diffractometer (Cu K α source, Rigaku Smartlab, Japan) to observe the crystal structure characteristics. In addition, Fourier transform infrared spectra were obtained on a Nicolet iS50 spectrometer (ThermoFisher Scientific, USA) with potassium bromide as the reference. Raman spectra were obtained using Micro Raman Spectroscopy system (Witech Alpha 300 R, Germany) with 523 nm Nd:YAG laser light, 5 mW power, and 600 groove mm diffraction grating. 2 μL of the suspension was spotted onto an Al-coated slide for Raman measurement in each sample. N_2 adsorption-desorption analysis was carried out by a gas adsorption analyzer (Micromeritics, ASAP 2020, USA) at -196°C . Several physical properties, including the specific surface area, the total pore volume, and the pore size distribution, were calculated with empirical formula (Brunauer-Emmett-Teller (BET) equation and Barrett-Joyner-Halenda (BJH) model, respectively). An XPS spectrometer (ThermoFisher Scientific, ESCALAB 250 Xi, USA) was utilized to analyze the surface chemical composition and corresponding valence state. All the binding energies were uniformly calibrated by the C 1 s peak position at 284.8 eV during the data processing.

The zeta potential values were measured by a Zetasizer instrument (Brookhaven, ZetaPALS, USA).

2.5. DFT calculation

The Vienna ab initio simulation package (VASP) was applied for the first-principle computations [19,34]. The correlation between ions and valence electrons was represented via the projector augmented wave (PAW) potentials, while the interelectronic exchange-correlation was processed under the generalized gradient approximation (GGA) in the Perdew-Burke-Ernzerhof (PBE) form [27]. The plane wave cutoff energy was adopted as 520 eV. A $2 \times 2 \times 2$ sheet k-point mesh was used to achieve accurate observed energy. Ionic relaxation analyses were performed under the conventional energy (10^{-4} eV) and force (0.01 eV/Å) convergence criteria. The adsorption energy (E_{ad}) of oxyanions, i.e., phosphate (HPO_4^{2-}) and arsenate (AsO_4^{3-}) groups, on the surface of the adsorbents (La-BTC, Zr-BTC, Zr/La-BTC) was calculated with Eq. (1):

$$E_{ad} = E_{\text{surf/anion}} - (E_{\text{surf}} + E_{\text{anion}}) \quad (1)$$

where E_{surf} and E_{anion} are the ground-state energies (0 K) of the substrate and anion, and $E_{\text{surf/anion}}$ is the energy of the complex integrated with the substrate and anion after adsorption.

Bader charge analysis was conducted to calculate the partial charge distributions of the adsorbate (phosphate/arsenate) and the surface. In the Bader analysis, the electron charge distribution from the DFT calculation was partitioned and assigned to individual atoms [30]. The differences in the partitioned charge before and after adsorption indicate charge transfer between the surface and adsorbate. A negative value for the net charge indicates that the atom unit acts as an electron acceptor.

3. Results and discussion

3.1. Structures and morphologies of Zr/La-BTC MOFs

The morphologies of the as-prepared Zr/La-BTC MOFs with different Zr/La ratios are shown on Fig. 1. The pristine La-BTC had a long stick-like morphology, while Zr-BTC was constructed by blocks of amorphous particles with a diameter of 10–50 μm (Fig. S1). Interestingly, bowknot-like products appeared when the La and Zr species were integrated to synthesize the Zr/La-BTC composites. The 0.1Zr/La-BTC and 0.3Zr/La-BTC composites showed uniform bowknot-like structures with narrow waists (ca. 5 μm) in the middle and two pyramid-like bundles (length: 12.16 μm ; diameter: 0.9 μm) spreading out on both sides (Fig. 1a). Notably, the ratio of La to Zr in the Zr/La-BTC composites plays a vital role in the resultant structure. The continuous increase in the Zr constituent results in the disappearance of the bowknot-like morphology. 0.5Zr/La-BTC was constructed by irregular cuboid rods with lengths of 10–50 μm and diameters of 2–10 μm (Fig. 1b and 1c). The above SEM analysis results indicate that the doping of Zr species in the La-BTC matrix can cause dramatic evolution of its original structure. A bowknot-like nanocomposite was developed under a suitable Zr doping amount. In contrast, the excessive introduction of Zr species into the La-BTC failed to generate a solid crystalline structure and resulted in the inevitable disintegration of the exquisite bowknot-like system.

The XRD patterns of the La-BTC and bimetal Zr-La systems are shown in Fig. 2. The principal peaks of the La-BTC were accurately indexed to the well-crystallized phase of $\text{La}(1,3,5\text{-BTC}) \cdot 6\text{H}_2\text{O}$ (JCPDS: 27–1704), which is consistent with previous research [45]. Herein, the crystal structure of the La-BTC belongs to space group Cc with a tricapped trigonal prismatic geometry. The La atom is coordinated with 1,3,5-BTC ligands through oxygen atoms

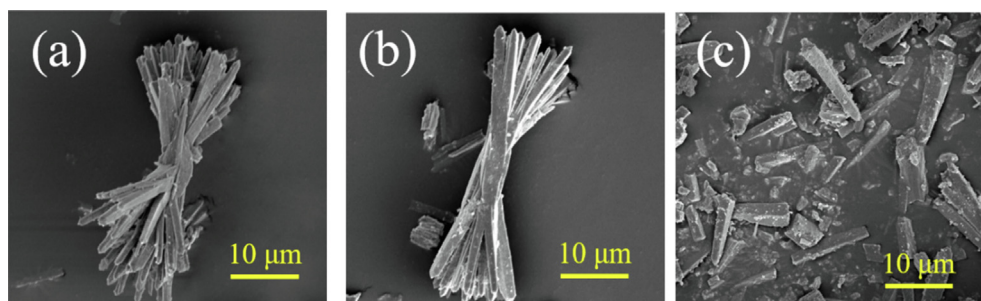


Fig. 1. SEM patterns of (a) 0.1Zr/La-BTC, (b) 0.3Zr/La-BTC, and (c) 0.5Zr/La-BTC.

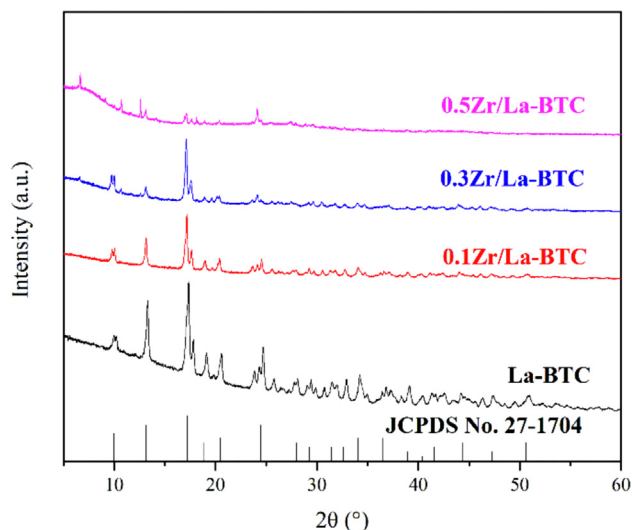


Fig. 2. XRD patterns of La-BTC and Zr/La-BTC MOFs.

from water molecules and carboxylate groups. For samples with small Zr doping amounts, 0.1Zr/La-BTC and 0.3Zr/La-BTC displayed prominent diffraction peaks similar to those of La-BTC, while the intensities of the characteristic peaks dropped to some extent. However, the crystalline structure of La-BTC crumbled when more Zr-based constituents were introduced. It can be observed that the 0.5Zr/La-BTC composite demonstrated an XRD pattern that was distinct from those of the other three samples as the characteristic peak at $2\theta = 17.2^\circ$ ($d = 5.14 \text{ \AA}$) disappeared. The phase transformation was probably attributed to the excessive introduction of Zr atoms leading to the collapse of the lattice of the La-BTC matrix. The discrepancy in the phase structure between 0.5Zr/La-BTC and the other two Zr/La-BTC samples also coincided nicely with the SEM results, where 0.5Zr/La-BTC displayed irregular brick-like particles instead of a bowknot-like morphology.

FTIR was carried out to analyze the surface functional groups of the as-prepared MOFs. As shown in Fig. 3a, all samples exhibited bands at 3396 cm^{-1} , assigned to the $-\text{OH}$ stretching vibration mode originating in H_2O molecules. In addition, bands assigned to the vibration of the aromatic skeleton of the benzene ring were also observed at 1611, 764, and 664 cm^{-1} [8]. Characteristic asymmetric and symmetric stretching vibrations of the carboxylate groups in the BTC ligand displayed bands at approximately 1556 and 1435 cm^{-1} , respectively [29]. The appearance of bands at 1611 and 1435 cm^{-1} represents characteristics of bridging coordination. The novel band that formed at 1651 cm^{-1} after Zr doping is attributed to the vibration of $\text{C}=\text{O}$ between BTC and Zr/La metals in

the frameworks of all three Zr/La-BTCs [33], suggesting that a coordination reaction occurs between Zr ions and the carboxyl groups. Two additional peaks centered at 726 and 713 cm^{-1} were identified, originating from the BTC benzene groups influenced by Zr substitution and connection with BTC ligands. This result indicates that the benzene groups in Zr/La-BTCs vary from those in La-BTC [20]. A small peak centered at 451 cm^{-1} suggests the Zr-O stretching vibration mode. The appearance of the peak at 937 cm^{-1} is probably attributed to the $\text{C}-\text{O}$ vibration because there are four carboxylic groups connected with Zr^{4+} .

No apparent differences were observed in the FTIR spectra of the three Zr/La-BTCs except for the intensity drop of the band at 530 cm^{-1} assigned to La-O vibrations with the increase of Zr doping amount. This result suggests that as more Zr atoms were introduced, La-relative peaks were weaker in the spectra. The evolution of the intensities of these peaks is consistent with the various Zr doping amounts in the precursor solutions. Microscopic images of 0.1Zr/La-BTC, 0.3Zr/La-BTC, and 0.5Zr/La-BTC (Fig. S2) detected by the WiTec confocal micro-Raman system exhibited the same morphology as the above SEM results. The corresponding Raman spectra are shown in Fig. 3b. Characteristic sharp bands at 1594, 1450, 1369, 1001, and 806 cm^{-1} are assigned to the ν_{asym} of the $\text{O}-\text{C}-\text{O}$ stretching, ν_{sym} of the $\text{O}-\text{C}-\text{O}$ stretching, ν_{sym} of the $\text{C}=\text{O}$ stretching, $\text{C}=\text{C}$ modes of the benzene ring and out-of-plane ring $\text{C}-\text{H}$ bending vibrations, respectively [22,43]. The occurrence of these five bands in the Raman spectra of the three Zr/La-BTC samples indicates that Zr doping does not cause the collapse of the fundamental organic framework of the La-BTC MOF. The coordination between metal atoms and organic ligands remains despite the change in central metal atoms. Thus, the data obtained from Raman spectra respond well to the above FTIR analysis results.

N_2 adsorption-desorption measurements illustrate that the introduction of Zr into the La-BTC matrix contributes to a dramatic increase in the specific surface area. Zr/La-BTC and 0.3Zr/La-BTC possess high surface areas of 90.12 and $80.90 \text{ m}^2/\text{g}$, approximately 8 times higher than La-BTC (Table S4). The results from SEM analysis indicate that 0.1Zr/La-BTC and 0.3Zr/La-BTC exhibit bowknot-like morphology with a narrow waist in the middle and two bundles of outspread long prisms at the ends. In contrast, La-BTC is constructed of long stick-like particles whose average diameter and length are almost parallel to those of 0.1Zr/La-BTC. Thus, it is concluded that 0.1Zr/La-BTC and 0.3Zr/La-BTC, which exhibit more subdivision prism structures, possess higher surface areas. However, the surface area of 0.5Zr/La-BTC, which is not constructed by a bowknot-like system, is only $9.74 \text{ m}^2/\text{g}$, indicating that the bowknot-like morphology is a significant factor for bimetal Zr/La MOFs to form a high surface area structure. The N_2 adsorption-desorption isotherm curves of 0.1Zr/La-BTC exhibit a type IV structure with an H3 hysteresis loop, as described by IUPAC [32]

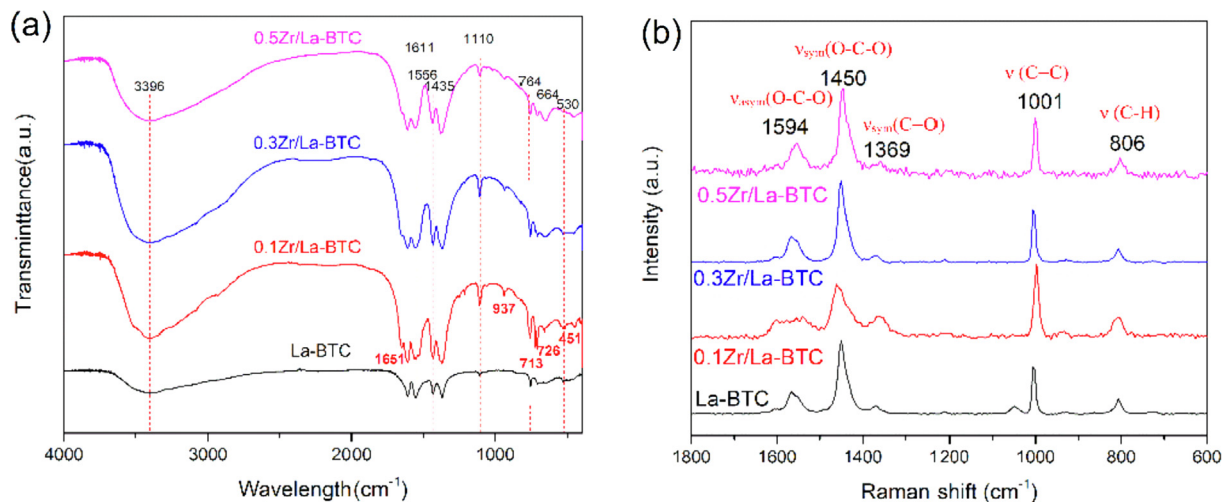


Fig. 3. (a) FTIR and (b) Raman spectra of La-BTC and Zr/La-BTC MOFs.

(Fig. S3), revealing that slit-shaped pores are formed during the aggregation of 0.1Zr/La-BTC particles.

3.2. Adsorption performance of the Zr/La-BTC MOFs

The phosphate and arsenate removal efficiencies of La-BTC, Zr-BTC, and Zr/La-BTC MOFs were evaluated at different initial concentrations. The adsorption isotherm results are shown in Fig. 4. Zr/La-BTC samples showed much superior P and As(V) adsorption efficiencies than pristine La-BTC and Zr-BTC. This result indicates that the introduction of Zr into La-BTC brings about significant improvement in the adsorption performance. Among the three Zr/La-BTCs, 0.1Zr/La-BTC demonstrated the highest adsorption capacities for both phosphate and arsenate, almost twice those of La-BTC and Zr-BTC. However, an improper Zr doping amount leads to the deterioration of the adsorption performance, as 0.5Zr/La-BTC failed to inherit the outstanding adsorption merits. The adsorption capacities of 0.5Zr/La-BTC remained at the same level as La-BTC and Zr-BTC.

The isotherm data were further fitted with the Langmuir and Freundlich models, and the corresponding fitting results for P and As(V) are displayed in Tables S5 and S6, respectively. The model correlation coefficients (R^2) of three Zr/La-BTC samples for both P and As(V) adsorption indicates that the Langmuir model fits

better than the Freundlich model. The higher correlation coefficient of the Langmuir model ($R^2 \approx 0.97$) implies that monolayer adsorption is dominant in the adsorbent-sorbate interactions. Similar results have been widely described in La- and Zr-based adsorbents [24,38]. Prior studies have noted that the b value in the Langmuir model shows a positive correlation with adsorption capacity [26]. The b value of La-BTC is similar to that of Zr-BTC, while that of 0.1Zr/La-BTC (0.23 L/g) is much higher. A similar phenomenon is also observed with the K_f and n values of the Freundlich model. According to the fitting results of the Langmuir model, the theoretical maximum adsorption capacity (Q_m) of 0.1Zr/La-BTC for phosphate and arsenate is 158.88 mg/g and 102.38 mg/g, respectively. Compared with those of many phosphate and arsenate scavengers developed in recent years (Table S7), the adsorption performance of 0.1Zr/La-BTC is highly competitive. Theoretically, the adsorption capacities of the Zr/La-BTC MOFs ought to be the approximate sum of the corresponding capacities of La-BTC and Zr-BTC multiplied by the percentage of Zr and La species added to the precursor solutions [26]. In that case, the capacities of 0.1Zr/La-BTC for P and As(V) adsorption are expected to be 79.59 mg/g and 48.45 mg/g, respectively (i.e. $0.9 \times Q_m \text{ La-BTC} + 0.1 \times Q_m \text{ Zr-BTC}$). However, the actual experimental data were 158.88 mg/g and 102.38 mg/g, far above the theoretical values. This result indicates that 0.1Zr/La-BTC is not constructed by

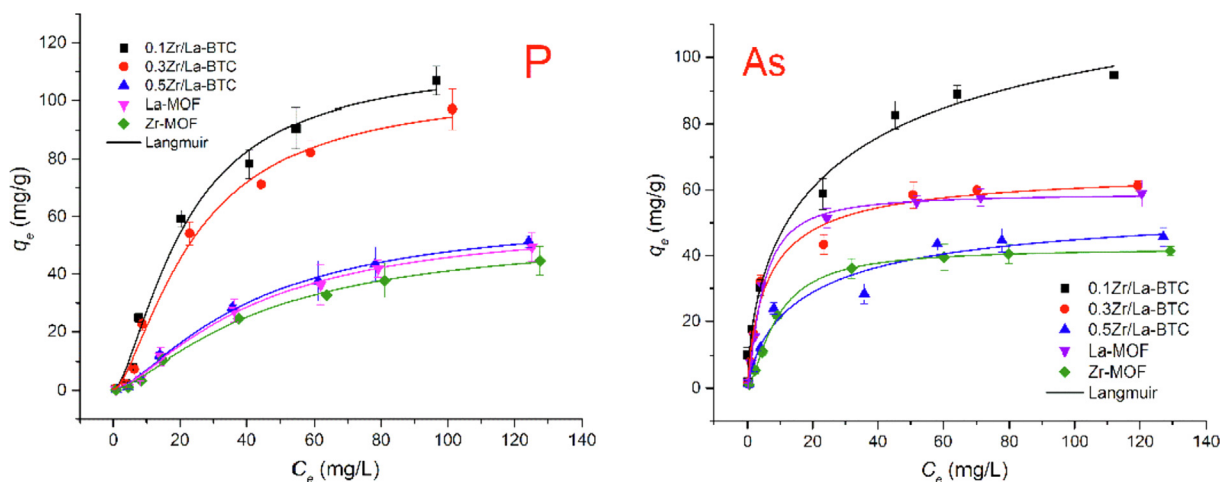


Fig. 4. Adsorption isotherms of phosphate and arsenate on La-BTC, Zr-BTC and Zr/La-BTC MOFs.

the physical assembly of La-BTC and Zr-BTC. Zr doping results in a fundamental structural change of La-BTC. According to the above structural characterization analysis, 0.1Zr/La-BTC is constructed from the central Zr/La atoms coordinated by 1,3,5-BTC ligands in which La and Zr species both have strong adsorption affinity to phosphate and arsenate. The specific Zr/La bimetal organic framework structure enhances adsorption forces for target anions.

The adsorption kinetics were investigated to evaluate the phosphate and arsenate uptake speed of Zr/La-BTC composites, and the results are displayed in Fig. 5. The phosphate and arsenate removal rates by 0.1Zr/La-BTC were much higher than those of La-BTC, Zr-BTC, and the other two Zr/La-BTC composites. Furthermore, large amounts of phosphate and arsenate anions were adsorbed rapidly once the adsorption process was launched, and nearly 80% of the maximum adsorption capacities were achieved in the initial 2 h. Finally, the adsorption equilibrium for phosphate and arsenate was reached at approximately 6 h and 12 h, respectively. The non-linear pseudo-first-order and pseudo-second-order models were used to fit the kinetic data [23]. The higher fitting degree (R^2) shown in Tables S8 and S9 indicates that the pseudo-second-order model is more accurate in describing the adsorption kinetics behavior, suggesting that the adsorption process was dominated by chemisorption [12]. It should be emphasized that the above isotherm and kinetics results reveal the great adsorption affinity of 0.1Zr/La-BTC for both phosphate and arsenate. Thus, 0.1Zr/La-BTC is discussed in detail in the following sections.

3.3. Effect of co-existing matters on adsorption

Ubiquitous anions in water environments usually coexist and compete for active sites on adsorbents. Thus, the effect of common anions (SO_4^{2-} , NO_3^- , HCO_3^- , Cl^- , F^-) on the adsorption of phosphate and arsenate on 0.1Zr/La-BTC was evaluated. As depicted in Fig. S4, the P and As(V) adsorption capacities demonstrated a downward trend with the increasing strength of the five anionic competitors. However, even for solutions with high concentrations of coexisting anions (50 mg/L), 0.1Zr/La-BTC still achieved nearly 80% of the initial adsorption capacities obtained in solutions containing only phosphate or arsenate. The selectivity factor (α) was calculated to quantify the influence of the coexisting anion [26] (Eqs. S2 and S3). The α value of 0.1Zr/La-BTC exhibited insignificant fluctuation with the occurrence of high concentrations of coexisting anions (Table S10). The negligible interference of coexisting anions on adsorption capacity indicates the remarkable inherent

affinity of 0.1Zr/La-BTC with La and Zr active sites toward phosphate and arsenate. Herein, the inner-sphere complex is probably the dominant interaction form, which is robust force insensitive to electrolyte addition [21]. The decrease in adsorption efficiency for target phosphate and arsenate is primarily attributed to the occupation of finite active sites by the coexisting anions.

3.4. Effect of pH on adsorption efficiency

pH is a factor that significantly influences the adsorption performance by altering the existing form of functional groups on the adsorbent and the speciation of the anionic adsorbate. The efficiencies of 0.1Zr/La-BTC on phosphate and arsenate adsorption in solutions with pH ranging from 3 to 10 were tested (Fig. S5). Acidic pH conditions are favorable for phosphate adsorption, and the best capacities are achieved at pH values from 4 to 6. However, the continuous increase in pH from 6 to 10 leads to a decline in the adsorption capacity. This phenomenon is consistent with other La- and Zr-based adsorbents [9,17,18]. According to Zeta potential analysis result (Fig. S6), the point of zero charge (pH_{pzc}) of 0.1Zr/La-BTC is 6.6. Thus, under acidic conditions of $\text{pH} < 6.6$, the surface of 0.1Zr/La-BTC was positively charged due to protonation. The negatively charged phosphate is accessible to be adsorbed due to the effect of electrostatic attraction. However, deprotonation occurs under higher pH conditions in which the surface of 0.1Zr/La-BTC becomes negatively charged, repelling the phosphate anions with the same negative charge. Additionally, a large number of hydroxide groups emerge in high pH solutions, exerting a remarkable competitive effect with phosphate anions for adsorption sites. Thus, these effects contributed to the deterioration of phosphate adsorption performance in alkaline solutions. However, arsenate adsorption is immune to drastic pH changes. A remarkable increase in adsorption capacity was observed in a pH range from 3 to 5 and remained high over the pH range of 6–10. The dominant species of As(V) is H_3AsO_4 at $\text{pH} < 4$, based on calculation results of MINTEQA 3.0 [46]. When the pH further increases, As(V) exists as anionic H_2AsO_4^- and then changes to HASO_4^{2-} and AsO_4^{3-} at $\text{pH} > 8.0$. Thus, it is hypothesized that the sharp adsorption capacity increase from 3 to 5 is mainly attributed to the enhanced electrostatic adsorption between negatively charged H_2AsO_4^- and positively charged 0.1Zr/La-BTC. Interestingly, the adsorption capacities were relatively high when the $\text{pH} > 8.0$. This phenomenon is possibly due to the fact that chemisorption, rather than electrostatic adsorption, acts as the dominant adsorption force under these pH

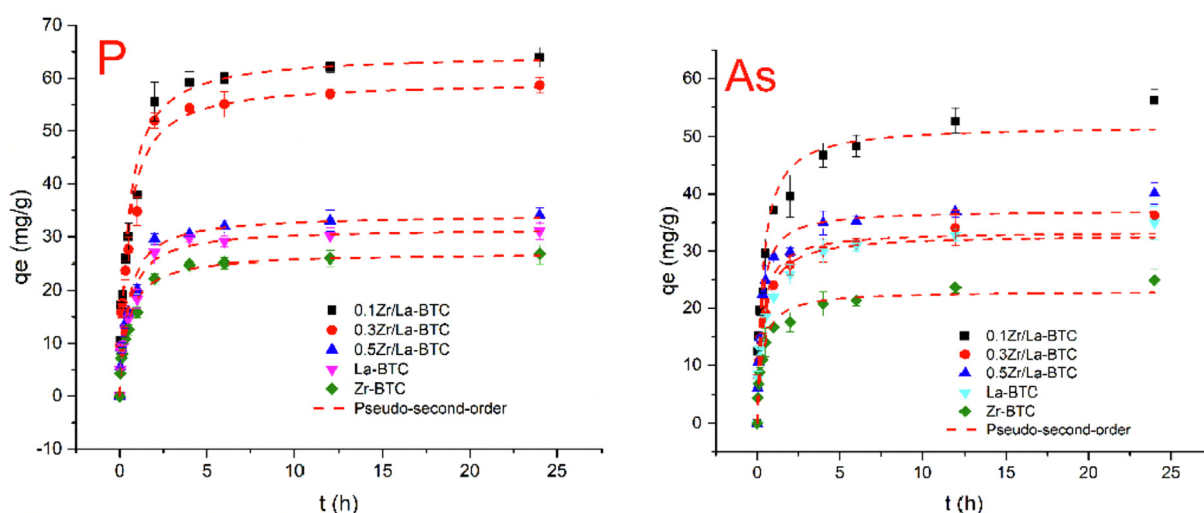


Fig. 5. Adsorption kinetics of phosphate and arsenate on La-BTC, Zr-BTC and Zr/La-BTC MOFs.

conditions, as confirmed by the pseudo-second-order kinetic model.

3.5. Adsorption mechanism

SEM-EDS elemental scanning mapping images of 0.1Zr/La-BTC after simultaneous phosphate and arsenate adsorption are illustrated in Fig. 6. The adsorption-saturated 0.1Zr/La-BTC retained its bow-like morphology, implying that the adsorption process does not damage to the external appearance of the 0.1Zr/La-BTC. La and Zr were both detected, indicating the primary bimetallic elemental composition of this composite. The color brightness of La was much higher than that of Zr due to the significant disparity between La and Zr in molar contents within the matrix. Apparent red and yellow dots related to P and As elements were homogeneously distributed throughout the bowknot-like particles. This result indicates that phosphate and arsenate were effectively adsorbed on the surface. Moreover, the homogeneous distribution of La, Zr, P and As elements indicates the uniform structural composition throughout the material after adsorption.

FTIR spectra of 0.1Zr/La-BTC before and after adsorption are shown in Fig. 7a. A distinct band attributed to the O–P–O bend vibration in PO_4^{3-} groups appeared at 611 cm^{-1} after P adsorption. In addition, the typical characteristic of the asymmetric stretch vibration of P–O was observed at 1051 cm^{-1} [45]. On the other hand, after As(V) adsorption, a new moderate band appeared at 836 cm^{-1} . This band is associated with the frequency of the As–O–M (M = La or Zr) band of the complexed arsenate [25]. These results suggest the effective capture of phosphate and arsenate on 0.1Zr/La-BTC and are consistent with the SEM-EDS analysis. Apparent intensity reduction of the bands at 457 and 663 cm^{-1} was observed in the spectra after both P and As adsorption, indicating the M–O bond contributes to phosphate and arsenate complexation. A similar observation was also found in previous literature [6]. It is suggested that the formation of Zr/La–O– PO_4 or Zr/La–O– AsO_4 species is accomplished during the adsorbent-adsorbate interactions.

To elucidate the enhanced P and As(V) adsorption efficiency of 0.1Zr/La-BTC, XPS analysis was carried out. The survey scan of 0.1Zr/La-BTC in Fig. 7b revealed peaks corresponding to the La 3p, Zr 3d, C 1s, and O 1s, identifying the main elemental composition as a La/Zr-based MOF. The appearance of P 2p and As 3d peaks after adsorption indicates that phosphate and arsenate anions were successfully captured. The atomic ratios of La and Zr calculated from XPS analysis were 4.72% and 0.54% (Table S11), respectively, close to the Zr/La ratio in the doping process. This

result indicates the adequate substitution of La atoms by Zr atoms to form Zr/La bimetallic MOFs. After adsorption, the atomic ratios of La and Zr both decreased, while the P and As proportions increased to 3.89% and 3.61%, respectively, suggesting that La and Zr atoms were overlaid with the adsorbed phosphate and arsenate. Interestingly, the atomic ratio of O rises slightly after adsorption. This result is somewhat counterintuitive from previous research concerning La/Zr-based adsorbents, where the replacement of hydroxide species is the predominant mechanism for oxyanion adsorption [26,29]. In that case, the proportion of O generally decreases after adsorption. The abnormal increase in the O atom ratio is mainly compensated by the new O atoms originating from phosphate and arsenate oxyanions captured via surface complexation.

The peaks of La 3d and Zr 3d in narrow spectra shift positively to higher binding energies after adsorption as depicted in Fig. 8. As the polarization interactions of aqueous H_2PO_4^- and AsO_4^{3-} were strong, the positive chemical shift indicates that the formation of H-bonded Zr/La... PO_4 or Zr/La... AsO_4 species plays a significant role in the adsorption reaction. This result is consistent with a previous report concerning Zr/La hydroxide. As mentioned in the literature, owing to the electronegativity difference of La and Zr, the incorporation of La and Zr oxides can induce an internal charge shuttle [40]. The internal electron transfer through the bridging O ligand primarily strengthens the formation of M... PO_4/AsO_4 (M = La or Zr) species. It is observed in Fig. 8 that novel peaks assigned to the La–O–Zr chemical state appeared in both the La 3d and Zr 3d high-resolution spectra after deconvolution [31]. All of the spectra were fitted using a Gaussian-Lorentzian peak shape. After adsorption, the integral area of La–O–Zr relative peaks decreases in both La 3d and Zr 3d spectra. The above results confirm that the bridging O ligands between La and Zr species play a crucial role in P and As adsorption. Based on MO theory analysis, the formation of M... PO_4/AsO_4 species (H-bond) is accompanied by charge transfer from the occupied orbitals of the adsorbent surface to the unoccupied orbitals in oxyanions. This charge transfer process was further confirmed via DFT calculation in the charge density deformation between the adsorbent surface and oxyanions as discussed later.

DFT calculations were performed to further elaborate on the adsorption mechanism and unveil the essential differences in phosphate and arsenate adsorption on bimetallic Zr/La-BTC MOFs with different Zr/La ratios. The optimized structures of the 0.1Zr/La-BTC and the binding complexes after adsorption are illustrated in Fig. 9. The adsorption energy (E_{ad}) of H_2PO_4^- for 0.1Zr/La-BTC was calculated to be -3.68 eV , while the values for 0.3Zr/La-BTC, 0.5Zr/La-BTC, La-BTC and Zr-BTC were calculated to be -3.37 , -2.21 ,

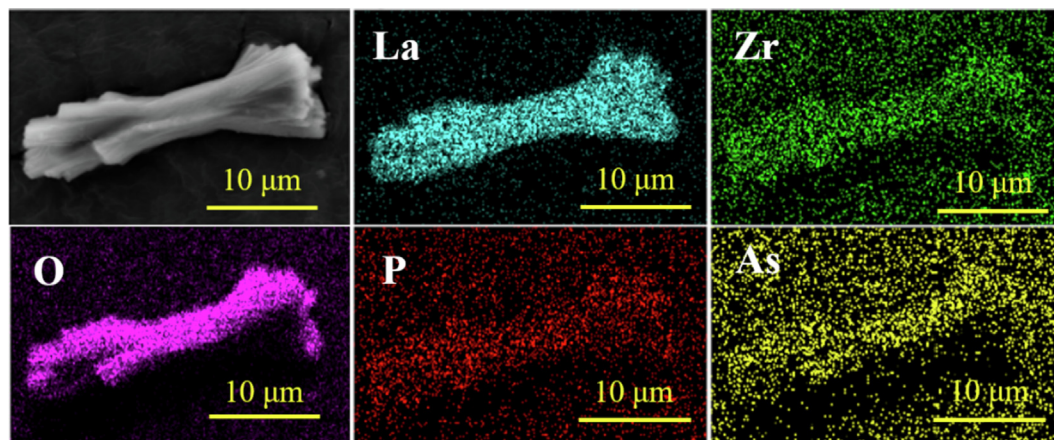


Fig. 6. SEM mapping of 0.1Zr/La-BTC after phosphate and arsenate adsorption.

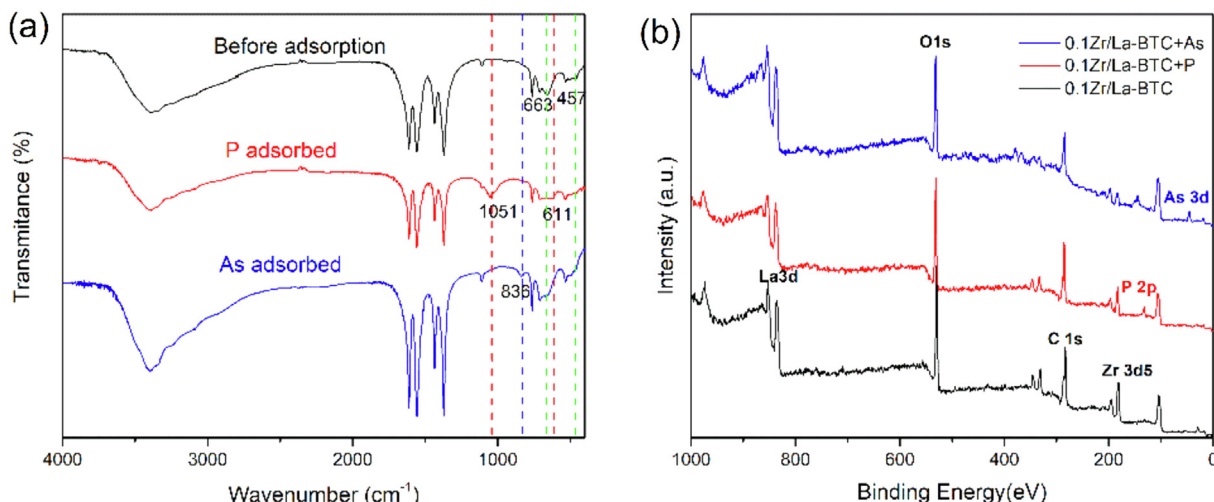


Fig. 7. (a) FTIR spectra and (b) XPS survey scan patterns of 0.1Zr/La-BTC after phosphate and arsenate adsorption.

–2.59, and –2.52 eV, respectively (Table S12). The negative E_{ad} values of these samples indicate that the adsorption of H_2PO_4^- is energetically spontaneous. In addition, a higher absolute value of E_{ad} represents stronger affinity of the adsorbent surface to the target anion in solution. Accordingly, the E_{ad} of H_2PO_4^- on the as-synthesized MOFs followed the sequence of $0.1\text{Zr/La-BTC} > 0.3\text{Zr/La-BTC} > 0.5\text{Zr/La-BTC} \approx \text{La-BTC} \approx \text{Zr-BTC}$. Similar results were also achieved for AsO_4^{3-} adsorption. 0.1Zr/La-BTC demonstrated the highest absolute value of E_{ad} for AsO_4^{3-} . It is worth noting that the absolute value of E_{ad} for AsO_4^{3-} is lower than that of H_2PO_4^- , indicating the obvious preference of Zr/La-BTC MOFs for phosphate rather than arsenate in adsorption affinity. These results obtained from the DFT theoretical calculation match well with the preceding data in batch adsorption experiments that 0.1Zr/La-BTC possesses the highest adsorption capacities for both phosphate and arsenate compared with unmodified La-BTC, Zr-BTC, and bimetallic Zr/La-BTC with higher Zr doping amounts. To the best of our knowledge, this is the first study to unveil and elucidate the significant role of Zr constituents in enhancing phosphate and arsenate adsorption on La-based MOFs.

To further elucidate the bonding nature between phosphate/arsenate groups and 0.1Zr/La-BTC , differential charge density ($\Delta\rho$) and Bader charge analyses of different adsorption configurations were performed. As shown in Fig. S7, yellow and cyan isosurfaces represent the accumulation and depletion of electron densities of oxyanions and coordinated Zr/La atoms. The different charge distributions between the 0.1Zr/La-BTC surface and oxyanions indicate that charge transformation occurs during adsorption. In the case of phosphate adsorption, the HPO_4^{2-} group accepts 0.78e from 0.1Zr/La-BTC after adsorption, while the coordinated La and Zr atoms are positively charged by donating 1.83 and 1.77 e, respectively. Similar results were also observed in the case of arsenate (AsO_4^{3-}) adsorption. The AsO_4^{3-} group gains electron density from the surface by 2.09 e after the adsorption reaction. The Bader charge analysis results suggest that electronic charges transform from the 0.1Zr/La-BTC surface to oxyanions during phosphate and arsenate adsorption.

The charge transformation is probably attributed to the back donation mechanism in which the electrons transform from the occupied orbitals of the adsorbent surface to the unoccupied orbitals in oxyanions. According to a previous study, owing to the electronegativity difference of La and Zr, the incorporation of La and Zr within the oxide-bonded matrix can induce an internal charge shuttle from La to Zr through the surrounding O 2p ligand

[40,49]. The as-induced internal electron shuttle in the bimetallic Zr/La-based material primarily strengthens the back donation interaction, bolstering the coordination between the metallic La/Zr atoms and oxyanions and leading to the formation of $\text{La/Zr}\cdots\text{PO}_4$ or $\text{La/Zr}\cdots\text{AsO}_4$ species [15]. The above differential charge density and Bader charge analysis further reveal the charge transfer process between the bimetallic Zr/La-based adsorbent and oxyanions, providing valuable insight for designing novel high-performance Zr/La-based adsorbents for capturing oxyanions.

3.6. Adsorbent regeneration

The results of batch adsorption/desorption experiments are illustrated in Fig. S8. For both phosphate and arsenate uptake, a decreasing trend in removal efficiency was observed with the increase in adsorption/desorption cycles. The loss of adsorption capacity is ascribed to the strong binding of the loaded oxyanions on the surface of 0.1Zr/La-BTC , which is resistant to treatment with alkaline regeneration agents. It is worth noting that over 70% of the initial adsorption capacities remained after four cumulative regeneration cycles, suggesting the relatively acceptable renewable ability of 0.1Zr/La-BTC . In that case, the adsorption capacity of 0.1Zr/La-BTC might be restored under suitable regeneration treatment, which is favorable for application in wastewater treatment due to its cost-effective performance at small doses.

3.7. Real water treatment efficiency

The applicability of 0.1Zr/La-BTC for natural water treatment was investigated. The initial total phosphorus concentration was adjusted to 4.9 mg/L to simulate the nature of domestic wastewater. As shown in Fig. S9, the P concentration was reduced to < 0.5 mg/L, and the As concentration was reduced to below 0.01 mg/L after treatment at a dose of 0.2 g/L. The treated water quality met the discharging standard of the USEPA and the World Health Organization's Guidelines for Drinking-Water Quality for inorganic arsenic [47]. The results suggest that 0.1Zr/La-BTC can remove phosphate and arsenate pollutants from a complex water environment containing competing matters.

4. Conclusions

Novel bimetallic Zr/La-BTC MOFs were synthesized under various Zr/La molar ratios for phosphate and arsenate removal from

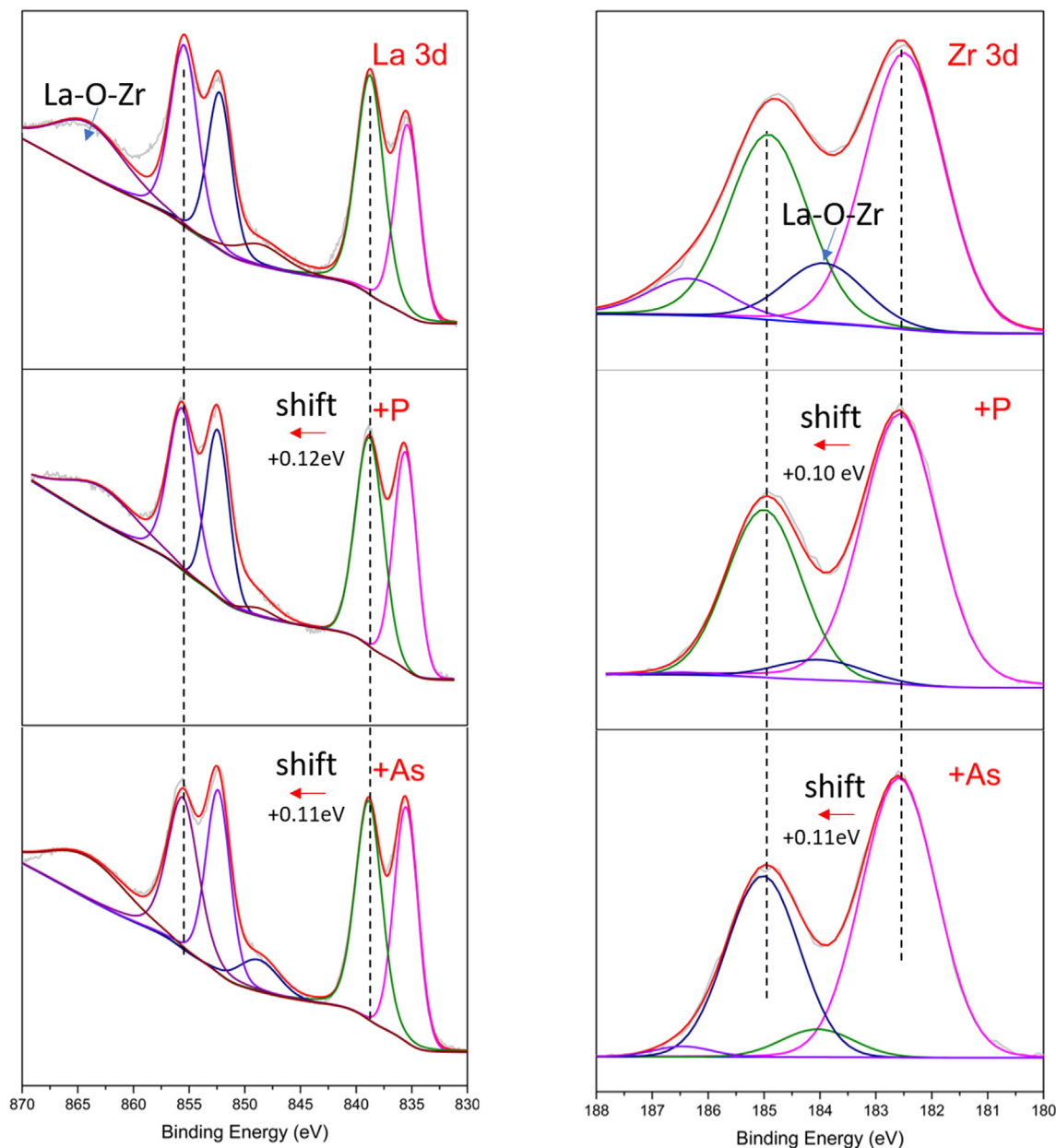


Fig. 8. XPS narrow spectra of La 3d and Zr 3d of 0.1Zr/La-BTC before and after P and As adsorption.

water. Physicochemical characterization showing exquisite bowknot-like morphology was obtained, and the specific surface area was dramatically increased compared with that of pristine La-BTC. The adsorption isotherm and kinetic results demonstrated the excellent adsorption performance of 0.1Zr/La-BTC, which achieved the maximum capacities of approximately 159 mg/g and 102 mg/g for phosphate and arsenate, respectively. The effects of pH change and coexisting anions on adsorption were insignificant. SEM-EDS, FTIR, and XPS analyses revealed the effective coordination between phosphate/arsenate and Zr/La species on the surface. The DFT calculation results revealed the adsorption affinity for phosphate and arsenate by ranking the adsorption energies as follows: 0.1Zr/La-BTC > 0.3Zr/La-BTC > 0.5Zr/La-BTC \approx La-BTC \approx Zr-BTC. This trend was consistent with the experimental data. The differential charge density and Bader charge analysis verified the electronic charge transformation from Zr/La atoms to phosphate/arsenate. The back-donation mechanism was hypothesized to be responsible for the superior adsorption capacity. This study

proposed a promising candidate and provided further insight into bimetallic Zr/La-based composites for the remediation of phosphate- and arsenate-bearing water.

Declaration of Competing Interest

The authors declare that they have no known competing financial interests or personal relationships that could have appeared to influence the work reported in this paper.

Acknowledgments

This study was supported by a project funded by the China Postdoctoral Science Foundation (No. 2020 M682778). Additional support was provided by the Leading Talents of Guangdong Province program (No. 2016LJ06N469), Open Project of State Key Laboratory of Urban Water Resource and Environment, Harbin

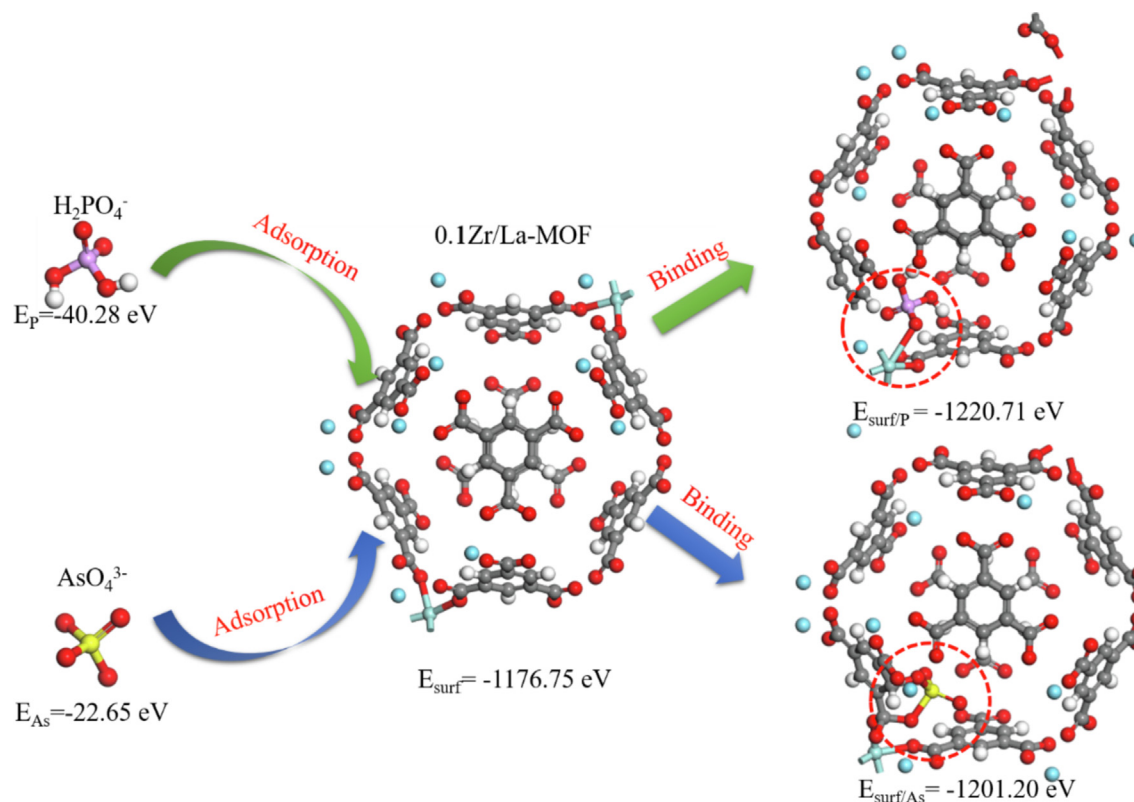


Fig. 9. DFT calculation of H_2PO_4^- and AsO_4^{3-} adsorption on the synthesized 0.1Zr/La-BTC.

Institute of Technology (No. QA202129). The authors acknowledge the assistance of SUSTech Core Research Facilities.

Appendix A. Supplementary material

Supplementary data to this article can be found online at <https://doi.org/10.1016/j.jcis.2022.01.033>.

References

- [1] I.W. Almanassra, G. McKay, V. Kochkodan, M. Ali Atieh, T. Al-Ansari, A state of the art review on phosphate removal from water by biochars, *Chem. Eng. J.* 409 (2021) 128211.
- [2] A. Bhatnagar, V.J. Vilar, C.M. Botelho, R.A. Boaventura, A review of the use of red mud as adsorbent for the removal of toxic pollutants from water and wastewater, *Environ. Technol.* 323 (2011) 231–249.
- [3] J. Cheng, K. Liu, X. Li, L. Huang, J. Liang, G. Zheng, G. Shan, Nickel-metal-organic framework nanobelt based composite membranes for efficient Sr^{2+} removal from aqueous solution, *Environ. Sci. Ecotechnol.* 3 (2020) 100035.
- [4] H. Chiew, M. Sampson, S. Huch, S. Ken, B.C. Bostick, Effect of groundwater iron and phosphate on the efficacy of arsenic removal by iron-amended biosand filters, *Environ. Sci. Technol.* 4316 (2009) 6295–6300.
- [5] P. Dhanasekaran, O. Sahu, Arsenate and fluoride removal from groundwater by sawdust impregnated ferric hydroxide and activated alumina (SFAA), *Groundwater Sustain. Develop.* 12 (2021) 100490.
- [6] L. Fang, Q. Shi, J. Nguyen, B. Wu, Z. Wang, I.M. Lo, Removal mechanisms of phosphate by lanthanum hydroxide nanorods: investigations using EXAFS, ATR-FTIR, DFT, and surface complexation modeling approaches, *Environ. Sci. Technol.* 5121 (2017) 12377–12384.
- [7] Farmer, A. 2018. Phosphate pollution: a global overview of the problem. *Phosphorus: Polluter and Resource of The Future—Removal and Recovery From Wastewater*; Schaum, C., Ed, 35–55.
- [8] J.-F. Feng, X. Yang, S.-Y. Gao, J. Shi, R. Cao, Facile and Rapid Growth of Nanostructured Ln-BTC Metal-Organic Framework Films by Electrophoretic Deposition for Explosives sensing in Gas and Cr^{3+} Detection in Solution, *Langmuir* 3350 (2017) 14238–14243.
- [9] H. Fu, Y. Yang, R. Zhu, J. Liu, M. Usman, Q. Chen, H. He, Superior adsorption of phosphate by ferrihydrite-coated and lanthanum-decorated magnetite, *J. Colloid Interface Sci.* 530 (2018) 704–713.
- [10] F. Haghseresht, S. Wang, D.D. Do, A novel lanthanum-modified bentonite, Phoslock, for phosphate removal from wastewaters, *Appl. Clay Sci.* 464 (2009) 369–375.
- [11] E.J. Hilkert Colby, T.M. Young, P.G. Green, J.L. Darby, Costs of Arsenic Treatment for Potable Water in California and Comparison to US Environmental Protection Agency Affordability Metrics 1, *JAWRA J. American Water Resour. Assoc.* 466 (2010) 1238–1254.
- [12] Y.S. Ho, G. McKay, A Comparison of Chemisorption Kinetic Models Applied to Pollutant Removal on Various Sorbents, *Process Saf. Environ. Prot.* 764 (1998) 332–340.
- [13] W. Huang, Y. Zhang, D. Li, Adsorptive removal of phosphate from water using mesoporous materials: A review, *J. Environ. Manage.* 193 (2017) 470–482.
- [14] J. Su, T. Lyu, H. Yi, L. Bi, G. Pan, Superior arsenate adsorption and comprehensive investigation of adsorption mechanism on novel Mn-doped $\text{La}_2\text{O}_3\text{CO}_3$ composites - ScienceDirect, *Chem. Eng. J.* 391 (2020) 123623, <https://doi.org/10.1016/j.cej.2019.123623>.
- [15] N. Khare, D. Hesterberg, J.D. Martin, XANES investigation of phosphate sorption in single and binary systems of iron and aluminum oxide minerals, *Environ. Sci. Technol.* 397 (2005) 2152–2160.
- [16] K.Y. Koh, Y. Yang, J.P. Chen, Critical review on lanthanum-based materials used for water purification through adsorption of inorganic contaminants, *Crit. Rev. Environ. Sci. Technol.* (2021) 1–52.
- [17] L. Kong, Y. Tian, Z. Pang, X. Huang, M. Li, R. Yang, N. Li, J. Zhang, W. Zuo, Synchronous phosphate and fluoride removal from water by 3D rice-like lanthanum-doped La@MgAl nanocomposites, *Chem. Eng. J.* 371 (2019) 893–902.
- [18] L. Kong, Y.u. Tian, Z. Pang, X. Huang, M. Li, N. Li, J. Zhang, W. Zuo, J. Li, Needle-like Mg-La bimetal oxide nanocomposites derived from periclase and lanthanum for cost-effective phosphate and fluoride removal: Characterization, performance and mechanism, *Chem. Eng. J.* 382 (2020) 122963, <https://doi.org/10.1016/j.cej.2019.122963>.
- [19] G. Kresse, J. Furthmüller, Efficiency of ab-initio total energy calculations for metals and semiconductors using a plane-wave basis set, *Comput. Mater. Sci.* 61 (1996) 15–50.
- [20] A. Laurikenas, A. Beganskiene, A. Kareiva, On the Synthesis and Characterization of Lanthanide Metal-Organic Frameworks, *Ceramics* 11 (2018) 54–64.
- [21] J. Li, B. Li, H. Huang, N. Zhao, M. Zhang, L. Cao, Investigation into lanthanum-coated biochar obtained from urban dewatered sewage sludge for enhanced phosphate adsorption, *Sci. Total Environ.* 714 (2020) 136839.
- [22] S. Li, K. Yang, C. Tan, X. Huang, W. Huang, H. Zhang, Preparation and applications of novel composites composed of metal-organic frameworks and two-dimensional materials, *Chem. Commun.* 528 (2016) 1555–1562.

- [23] J. Lin, L. Wang, Comparison between linear and non-linear forms of pseudo-first-order and pseudo-second-order adsorption kinetic models for the removal of methylene blue by activated carbon, *Front. Environ. Sci. Eng. China* 33 (2009) 320–324.
- [24] H. Liu, W. Guo, Z. Liu, X. Li, R. Wang, Effective adsorption of phosphate from aqueous solution by La-based metal-organic frameworks, *RSC Adv.* 6107 (2016) 105282–105287.
- [25] J.S. Markovski, D.D. Marković, V.R. Đokić, M. Mitrić, M.D. Ristić, A.E. Onjia, A.D. Marinković, Arsenate adsorption on waste eggshell modified by goethite, α - MnO_2 and goethite/ α - MnO_2 , *Chem. Eng. J.* 237 (2014) 430–442.
- [26] X. Min, X. Wu, P. Shao, Z. Ren, L. Ding, X. Luo, Ultra-high capacity of lanthanum-doped UiO-66 for phosphate capture: Unusual doping of lanthanum by the reduction of coordination number, *Chem. Eng. J.* 358 (2019) 321–330.
- [27] J.P. Perdew, K. Burke, M. Ernzerhof, Generalized gradient approximation made simple, *Phys. Rev. Lett.* 7718 (1996) 3865.
- [28] M.R. Pokhrel, B.R. Poudel, R.L. Aryal, H. Paudyal, K.N. Ghimire, Removal and recovery of phosphate from water and wastewater using metal-loaded agricultural waste-based adsorbents: a review, *J. Inst. Sci. Technol.* 241 (2019) 77–89.
- [29] S.M. Prabhu, S. Imamura, K. Sasaki, Mono-, Di-, and Tricarboxylic Acid Facilitated Lanthanum-Based Organic Frameworks: Insights into the Structural Stability and Mechanistic Approach for Superior Adsorption of Arsenate from Water, *ACS Sustain. Chem. Eng.* 77 (2019) 6917–6928.
- [30] E. Sanville, S.D. Kenny, R. Smith, G. Henkelman, Improved grid-based algorithm for Bader charge allocation, *J. Comput. Chem.* 285 (2007) 899–908.
- [31] D. Sarma, P.V. Kamath, C. Rao, Satellites in the X-ray photoelectron spectra of transition-metal and rare-earth compounds, *Chem. Phys.* 731–2 (1982) 71–82.
- [32] K.S. Sing, R.T. Williams, Physisorption hysteresis loops and the characterization of nanoporous materials, *Adsorption Sci. Technol.* 2210 (2004) 773–782.
- [33] Y. Sun, M. Amsler, S. Goedecker, A. Caravella, M. Yoshida, M. Kato, Surfactant-assisted synthesis of large Cu-BTC MOF single crystals and their potential utilization as photodetectors, *CrystEngComm* 2126 (2019) 3948–3953.
- [34] Y. Surendranath, M.W. Kanan, D.G. Nocera, Mechanistic studies of the oxygen evolution reaction by a cobalt-phosphate catalyst at neutral pH, *J. Am. Chem. Soc.* 13246 (2010) 16501–16509.
- [35] S. Thathsara, A.T. Cooray, D.R. Ratnaweera, T.K. Mudiyansele, A novel tri-metal composite incorporated polyacrylamide hybrid material for the removal of arsenate, chromate and fluoride from aqueous media, *Environ. Technol. Innovat.* 14 (2019) 100353.
- [36] C. Wang, J. Luan, C. Wu, Metal-organic frameworks for aquatic arsenic removal, *Water Res.* 158 (2019) 370–382.
- [37] C. Wang, X. Liu, J.P. Chen, K. Li, Superior removal of arsenic from water with zirconium metal-organic framework UiO-66, *Sci. Rep.* 51 (2015) 16613.
- [38] L. Wang, X. Wen, J. Li, P. Zeng, Y. Song, H. Yu, Roles of defects and linker exchange in phosphate adsorption on UiO-66 type metal organic frameworks: Influence of phosphate concentration, *Chem. Eng. J.* 405 (2021) 126681, <https://doi.org/10.1016/j.cej.2020.126681>.
- [39] Y. Wang, Y. Liu, T. Guo, H. Liu, J. Li, S. Wang, X. Li, X. Wang, Y. Jia, Lanthanum hydroxide: a highly efficient and selective adsorbent for arsenate removal from aqueous solution, *Environ. Sci. Pollut. Res.* 2734 (2020) 42868–42880.
- [40] C. Xiang, H. Wang, Q. Ji, G. Zhang, J. Qu, Tracking Internal Electron Shuttle Using X-ray Spectroscopies in La/Zr Hydroxide for Reconciliation of Charge-Transfer Interaction and Coordination toward Phosphate, *ACS Appl. Mater. Interf.* 1127 (2019) 24699–24706.
- [41] M.K. Yadav, D. Saidulu, A.K. Gupta, P.S. Ghosal, A. Mukherjee, Status and management of arsenic pollution in groundwater: A comprehensive appraisal of recent global scenario, human health impacts, sustainable field-scale treatment technologies, *J. Environ. Chem. Eng.* 105203 (2021).
- [42] A.A. Yakout, Z.A. Khan, High performance Zr-MnO₂@reduced graphene oxide nanocomposite for efficient and simultaneous remediation of arsenates As(V) from environmental water samples, *J. Mol. Liq.* 334 (2021) 116427, <https://doi.org/10.1016/j.molliq.2021.116427>.
- [43] J.-Y. Ye, C.-J. Liu, Cu₃(BTC)₂: CO oxidation over MOF based catalysts, *Chem. Commun.* 477 (2011) 2167–2169.
- [44] H. Yin, P. Yang, M. Kong, W. Li, Use of lanthanum/aluminum co-modified granulated attapulgite clay as a novel phosphorus (P) sorbent to immobilize P and stabilize surface sediment in shallow eutrophic lakes, *Chem. Eng. J.* 385 (2020) 123395, <https://doi.org/10.1016/j.cej.2019.123395>.
- [45] X. Zhang, F. Sun, J. He, H. Xu, F. Cui, W. Wang, Robust phosphate capture over inorganic adsorbents derived from lanthanum metal organic frameworks, *Chem. Eng. J.* 326 (2017) 1086–1094.
- [46] Y. Zhang, L. Wang, J. Chen, Y. Zhao, Y. Lai, P. Wu, Methodology of spatial risk assessment for arsenic species associated with sampling and analysis results optimization, *Sci. Total Environ.* 639 (2018) 8–18.
- [47] Y. Zheng, Global solutions to a silent poison, *Science* 3686493 (2020) 818–819.
- [48] Y. Zhi, C. Zhang, R. Hjorth, A. Baun, O.W. Duckworth, D.F. Call, D.R.U. Knappe, J. L. Jones, K. Grieger, Emerging lanthanum (III)-containing materials for phosphate removal from water: A review towards future developments, *Environ. Int.* 145 (2020) 106115, <https://doi.org/10.1016/j.envint.2020.106115>.
- [49] Y. Zhou, X. Guan, H. Zhou, K. Ramadoss, S. Adam, H. Liu, S. Lee, J. Shi, M. Tsuchiya, D.D. Fong, Strongly correlated perovskite fuel cells, *Nature* 5347606 (2016) 231–234.